Hindawi
International Journal of Rotating Machinery
Volume 2024, Article ID 6648925, 16 pages
https://doi.org/10.1155/2024/6648925

Research Article

Research on Demagnetization Fault Diagnosis Method of Mine Cutting Permanent Magnet Synchronous Motor

Guo Ye,[1] Yanbin Lu,[1] Jinyong Ju,[2] and Lianchao Sheng[1]

[1]*School of Mechatronic Engineering, Jiangsu Normal University, Xuzhou 221116, China*
[2]*School of Mechatronic Engineering, Anhui Polytechnic University, Wuhu 241000, China*

Correspondence should be addressed to Lianchao Sheng; shenglianchao@163.com

Received 3 April 2023; Revised 29 August 2023; Accepted 23 December 2023; Published 12 January 2024

Academic Editor: Paolo Pennacchi

To give timely and accurate diagnosis in the early stage of demagnetization failure for effective control and treatment, based on wavelet packet analysis, principal component analysis (PCA) dimensionality reduction, and least squares support vector machine(LSSVM), the extraction of features and the classification of demagnetization faults are completed. Since it is difficult to collect real data sets of demagnetization faults in practice, a two-dimensional finite element simulation model of permanent magnet synchronous motor (PMSM) under uniform demagnetization and partial demagnetization faults is established based on the Maxwell simulation platform. The wavelet packet analysis is used to extract the demagnetization feature of the A-phase current of the PMSM. Based on PCA dimensionality reduction, the dimensionality reduction of fault features is realized. The LSSVM is used to identify the fault and complete the fault classification. The simulation results show that the method has a high classification accuracy rate for demagnetization faults.

1. Introduction

At present, there are still many challenges to directly apply PMSM to mining machinery, especially shearer cutting transmission systems with high-end loads and large impacts. The risk of demagnetization of permanent magnets in PMSM is a common concern [1]. The shearer cutting transmission system has complex and changeable operating conditions such as large starting torque, strong vibration and shock, long operating time, and harsh heat dissipation conditions [2, 3], which will also lead to local demagnetization and irreversible demagnetization of the permanent magnets [1, 4]. After the motor is demagnetized, the vibration will increase and the performance will be degraded. In addition, after the permanent magnet demagnetization, the three-phase current of the PMSM will change. The demagnetization feature of permanent magnet can be extracted from the three-phase current and used for the early diagnosis of demagnetization fault. Corresponding measures can be taken to restore the magnetic properties of permanent magnets. At the same time, it can provide guidance for the subsequent application parameter setting of permanent magnet motor. Therefore, it is an important reality significance for protecting the motor to study the demagnetization fault monitoring method of the permanent magnet drive system in the shearer.

A group of scholars and institutions have carried out research on the demagnetization of PMSM. In order to diagnose motor demagnetization faults, researchers have studied the characteristics of demagnetization faults from different angles [5–7]. Urresty et al. [8] believe that when the motor is partially demagnetized, the copper loss will increase. The research of Ruoho et al. [9] showed that the PMSM is prone to demagnetization phenomenon due to the combined action of electrical, thermal, and mechanical stress and environmental problems. The output torque generated by the magnetic field is greatly reduced when the motor is demagnetized. Some scholars have also tested the back EMF, torque ripple, and zero-sequence voltage of the PMSM under the demagnetization fault [10, 11]. Zhu et al. [12] introduced the Vold-Kalman filter order to track the torque ripple of PMSM, extracted characteristic parameters. When a PMSM has demagnetization fault, the stator current of the motor

Table 1: Simulation parameters.

Parameter	Value	Unit	Parameter	Value	Unit
Number of pole pairs	8		Rotating speed	400	r/min
Phase	3		Working frequency	26.7	Hz
Operating temperature	75	˚C	Remanence	1.23	T
Permanent magnet material	NdFe35	H/m	Magnetization thickness	16.2	mm
Air gap length	3	mm	Rated torque	5	kNm
Rated current	107	A	Stator outer radius	300	mm
Rotor radius	183	mm	Air gap	1	mm

will generate specific harmonics [13], but this method is difficult to distinguish from an eccentric fault. Espinosa et al. [14] used the Hilbert-Huang transform to perform steady-state and dynamic analysis of the stator current at low, medium, and high speed changes. Ebrahimi and Faiz [15] directly detected the torque signal and selected two indicators, the amplitude of the sideband component in frequency and the radius of gyration, to estimate the degree of demagnetization failure. Urresty et al. [16] analyzed the torque effect, using two self-mixing laser diodes to measure the displacement of the shaft. The degree of demagnetization can be judged according to the magnitude of the shaft displacement. Bisschop et al. [17] estimated the susceptibility of permanent magnets based on the actual measured current, voltage, and motor structure parameters to monitor the degree of demagnetization failure. Li et al. [18] proposed a new fault diagnosis method of rolling bearing based on wavelet packet analysis and deep forest algorithm. Xiong et al. [19] proposed a bearing fault diagnosis method based on wavelet packet transform and DRN lightweight variant multibranch depth residual network. Zhao et al. [20] proposed a fault diagnosis method based on wavelet packet distortion and convolutional neural networks. In order to improve the accuracy of engine valve clearance fault diagnosis, Kuai and Huang [21] proposed a fault identification algorithm based on wavelet packet decomposition and artificial neural network. Krichen et al. [22, 23] proposed a two-step analysis study dealing with both uniform and partial demagnetization and studied the combined static eccentricity and the partial demagnetization faults in a permanent magnet synchronous motor. Haddad et al. [24] used a two-dimensional finite element analysis to model and simulate machine tools in health and fault states and performed fast Fourier transform to obtain the spectrum of phase voltage or current signals, which was used as a detailed feature of the classifier for fault detection. Fitouri et al. [25] proposed an interturn fault detection technique based on fast Fourier transform analysis of stator current and electromagnetic torque. Zhang et al. [26] propose a new method for diagnosing mechanical unbalance faults in permanent magnet synchronous motors and eliminate the fundamental components of the motor current fast Fourier transform results by Parker vector. Song et al. [27] used fast Fourier transform spectrum analysis to detect the correlation frequency of bearing outer raceway faults. However, there are few researches on demagnetization fault diagnosis using wavelet packet.

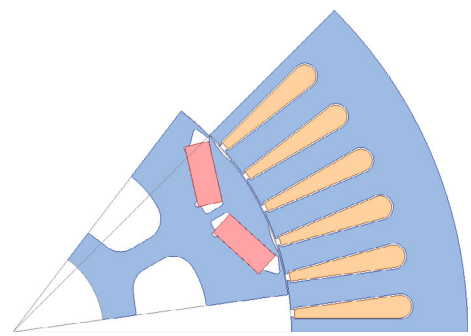

Figure 1: Two-dimensional model.

Ishikawa and Igarashi [28] simulated a partial loss of field failure by cutting a single permanent magnet and replacing a part of the cut with a nonpermanent magnet material. Zhu et al. [29], based on the noise signal, proposed a method to detect the demagnetization of permanent magnets by means of neural network, so as to realize the detection of PMSM uniform demagnetization diagnosis. At present, most of the pattern recognition of loss-of-excitation faults is aimed at the classification between loss-of-excitation faults and other faults, and there are few studies on the judgment of partial and uniform loss of excitation of motors.

Therefore, the research on demagnetization faults of mining PMSM will be developed. To reduce the cost, the data used in the demagnetization failure research adopts the simulation data. The two-dimensional simulation model of PMSM under normal state, uniform demagnetization, and partial demagnetization fault types is established by using Maxwell, and the current changes of the motor under different demagnetization fault types are analyzed. Demagnetization characteristic quantities of different demagnetization fault types are characterized. Finally, the classification of demagnetization characteristic quantities under different demagnetization fault types is realized based on PCA dimensionality reduction and LSSVM.

2. Finite Element Model of Demagnetization Fault

The demagnetization failure of PMSM means that the motor has suffered irreversible damage. The study of different degaussing faults needs many sets of experimental equipment and the cost is huge. Therefore, this kind of research

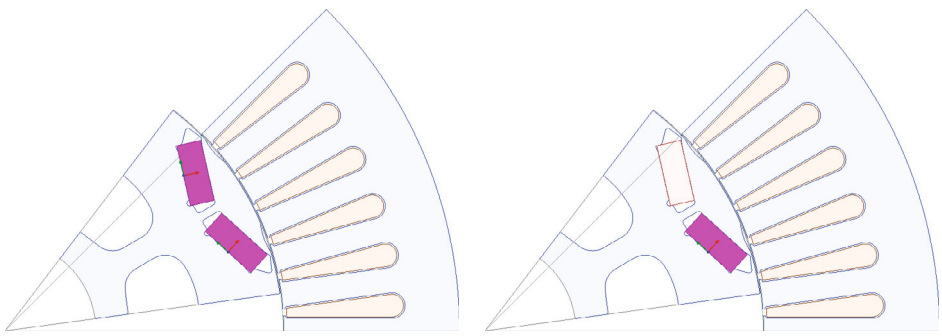

(a) Uniform demagnetization (b) Partial demagnetization

Figure 2: Finite element model of demagnetization failure.

is generally based on simulation data. The finite element method based on Maxwell software is a good method to simulate demagnetization faults. It can handle various complex mechanical problems and obtain more accurate results. To simulate different types of demagnetization faults, the two-dimensional simulation models of PMSM under different types of demagnetization faults are established with the help of Ansys Maxwell software.

Based on Maxwell's differential equation shown in equation (1), the electromagnetic field is analyzed by discrete finite element analysis and matrix solution, which has the advantages of high precision, convenient solution, and good convergence.

$$\begin{cases} \nabla \times H = J + \dfrac{\partial D}{\partial t}, \\ \nabla \times E = -\dfrac{\partial B}{\partial t}, \\ \nabla \times D = \rho, \\ \nabla \times B = 0, \end{cases} \tag{1}$$

where D is the electrical displacement and ρ is the charge density.

The following assumptions are made for the PMSM.

(1) The influence caused by the displacement current is ignored. (2) The eddy current effects in the iron core and armature windings are ignored, and the magnetic field is equivalent to a quasisteady field. (3) The influence of magnetic flux leakage at the end of the stator and rotor is not considered. (4) The material used in the motor is isotropic and uniformly distributed, ignoring the change of magnetic permeability with temperature.

The vector magnetic potential of the two-dimensional transient field solution domain of PMSM is represented by A_Z, and then, the field domain Ω needs to satisfy the following boundary value problem.

$$\begin{cases} W(A_Z) = \iint \left\{ \dfrac{1}{2\mu} \left[\left(\dfrac{\partial A_Z}{\partial x} \right)^2 + \left(\dfrac{\partial J_Z}{\partial x} \right)^2 \right] - A_Z J_Z \right\} dxdy = \min, \\ A_Z|_{\Gamma_1, \Gamma_2} = 0, \end{cases} \tag{2}$$

where J_Z is the conduction current density and Γ_1 and Γ_2 are the outer boundaries of the stator and rotor in the motor solution domain Ω, respectively.

According to the shape and size of each component of the motor, the motor model is drawn by related engineering drawing software such as AutoCAD and imported into Maxwell software, and the required motor finite element model is generated by setting the excitation source, boundary conditions, meshing method, and solution method.

The parameters of the PMSM are listed in Table 1.

The model of the PMSM is shown in Figure 1.

Since the demagnetization fault is measured according to the coercive force value of the permanent magnets, in the uniform demagnetization fault model, the coercive force of all permanent magnets is reduced by 25% to simulate the uniform demagnetization fault at 25% demagnetization degree, as shown in Figure 2(a). Second, the 1/2 permanent magnets in the motor were replaced with air to simulate a partial demagnetization fault at 25% demagnetization degree, as shown in Figure 2(b). The red area represents the demagnetized permanent magnet.

The model is set to start running under constant torque load and 1330 V working voltage. The simulation time is 2 s, and the data after stable operation is taken for analysis. Figures 3 and 4 are the magnetic density diagram and the A-phase current diagram under the normal state, uniform demagnetization, and partial demagnetization, respectively.

Figure 3 shows that when the motor is uniformly demagnetized, the magnetic density decreases as a whole, and the color becomes lighter; when the motor is partially demagnetized, the color of the permanent magnet in the demagnetized part turns blue. When the motor is in a normal state, the motor stator current amplitude is about 260 A, and when the motor is demagnetized, the motor current amplitude increases to a certain extent. When the motor loses magnetism, specific harmonics will appear in the A-phase current of the motor, and the greater the degree of fault, the more obvious the harmonic content, but the proportion of the fault component harmonics is not large. The accuracy of fault diagnosis by the method of judging specific harmonic content is not high. Therefore, the demagnetization characteristic quantity is extracted from the A-phase current by wavelet packet analysis.

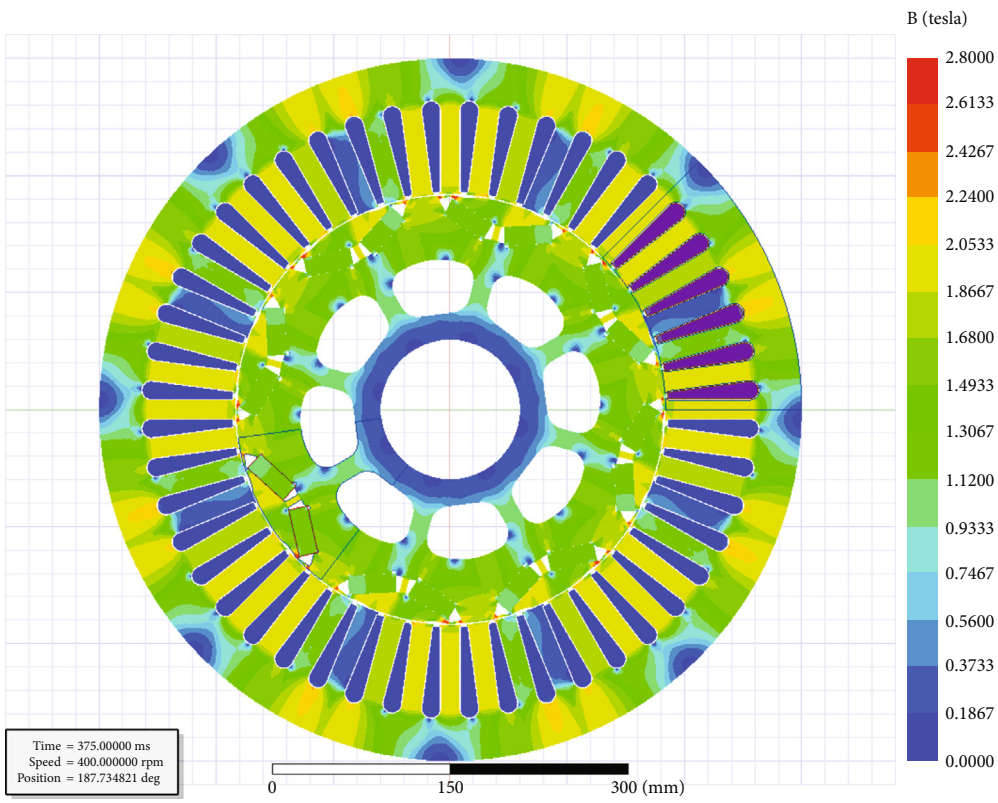

(a) Normal status

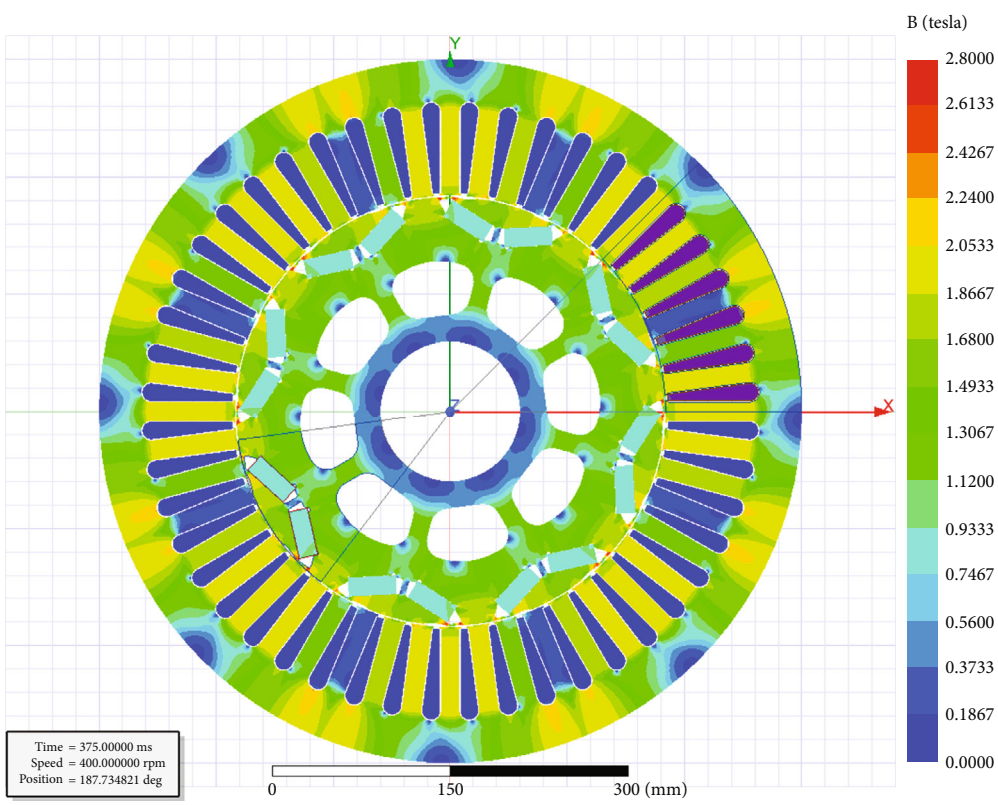

(b) Uniform demagnetization

Figure 3: Continued.

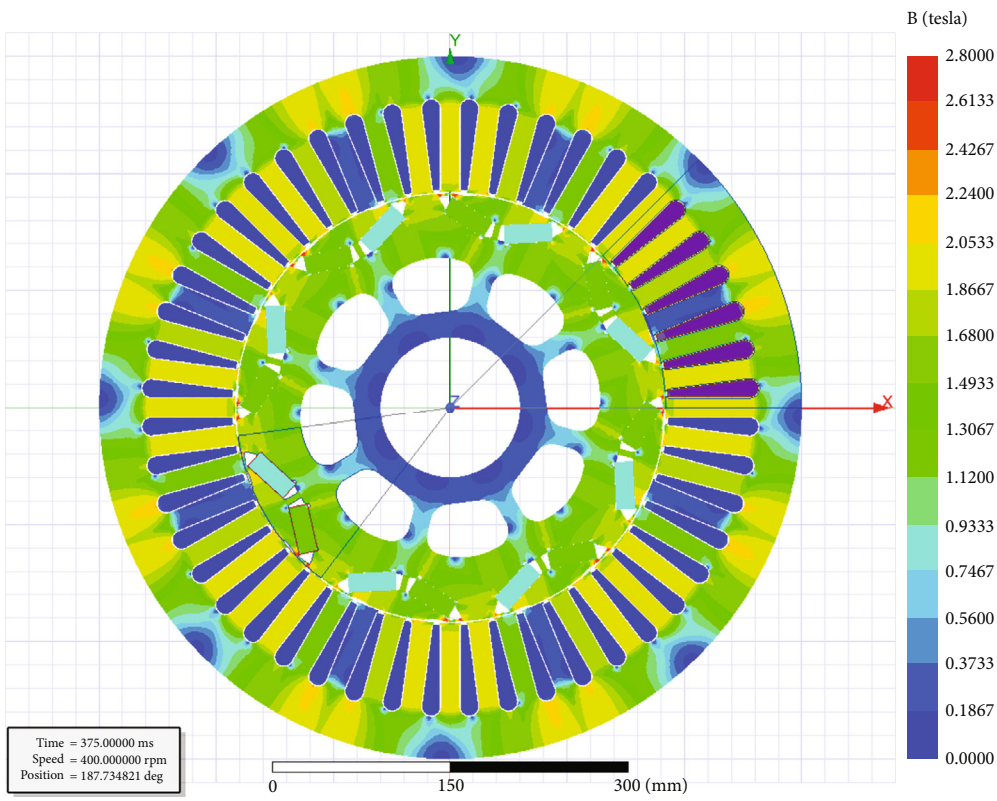

(c) Partial demagnetization

Figure 3: Magnetic density map.

3. Demagnetization Fault Feature Extraction

To improve the signal processing accuracy and remove the influence of current amplitude, the signal is decomposed into each frequency band by wavelet packet analysis, and the energy value of each frequency band is calculated, and the eigenvector is obtained after normalization. Compared with wavelet transform, wavelet packet analysis can subdivide the high-frequency part and the low-frequency part more effectively, and the signal processing accuracy is higher.

3.1. Principle of Wavelet Packet Analysis. Based on wavelet packet analysis, the feature extraction of loss of magnetic field is carried out. The function ω_n satisfies

$$\begin{cases} \omega_{2n}(t) = \sqrt{2}\sum_k h_n \omega_n(2t-k), \\ \omega_{2n+1}(t) = \sqrt{2}\sum_k g_n \omega_n(2t-k). \end{cases} \tag{3}$$

The relationship between h_n and g_n is as follows:

$$\begin{cases} \sum_n h_n = \sqrt{2}, \\ \sum_n h_{n-2k} h_{n-2l} = \delta_{kl}, \\ g_n = (-1)^n h_{1-n}. \end{cases} \tag{4}$$

$L(R)^2 = \oplus W_J$, $J \in Z$; W_J wavelet packet analysis will decompose the arbitrary subspace expression as U_{j-k}^{2k+mg}. The corresponding canonical orthonormal basis is $\{2^{(j-k)/2}\omega_n 2^{j-k} t - l, n = 2^k + m, l \in Z\}$. The variables j and k are scale parameters. m is the mth frequency band. n is the frequency parameter. The wavelet packet coefficients can be solved according to

$$\begin{cases} d_i^{j,2n} = \sum_k \bar{h}_{k-2l} d_k^{j+1,n}, \\ d_i^{j,2n+1} = \sum_k \bar{g}_{k-2l} d_k^{j+1,n}. \end{cases} \tag{5}$$

The decomposition process is shown in Figure 5.

The wavelet packet decomposition filter is G and H, where G is related to $\Phi_j(t)$ and H is related to the scale. The algorithm is

$$\begin{cases} p_0^1(t) = f(t), \\ p_j^{2i-1} = \sum_k H(k-2t) p_{j-1}^i(t), \\ p_j^{2i} = \sum_k \mathrm{G}(k-2t) p_{j-1}^i(t). \end{cases} \tag{6}$$

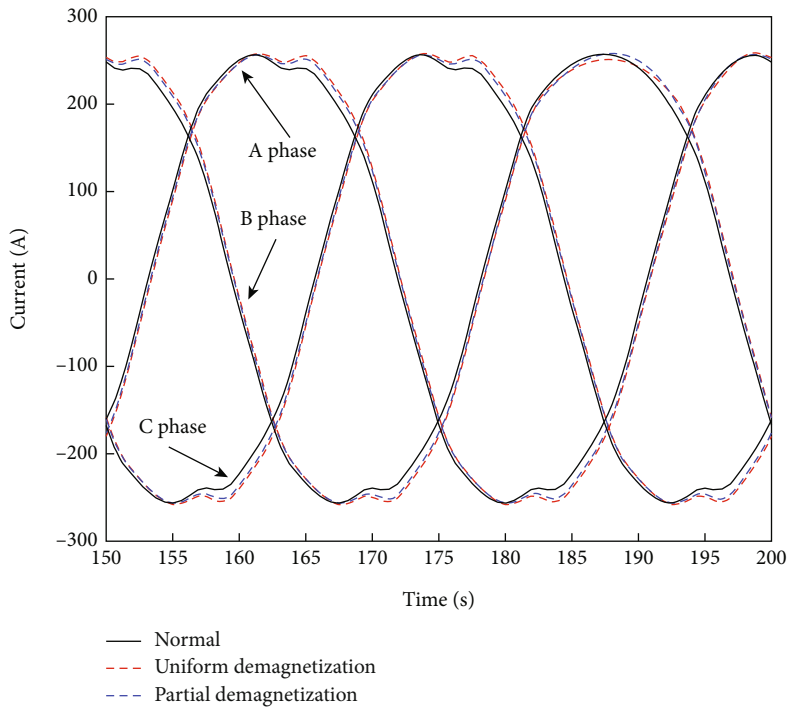

Figure 4: Three-phase current of motor.

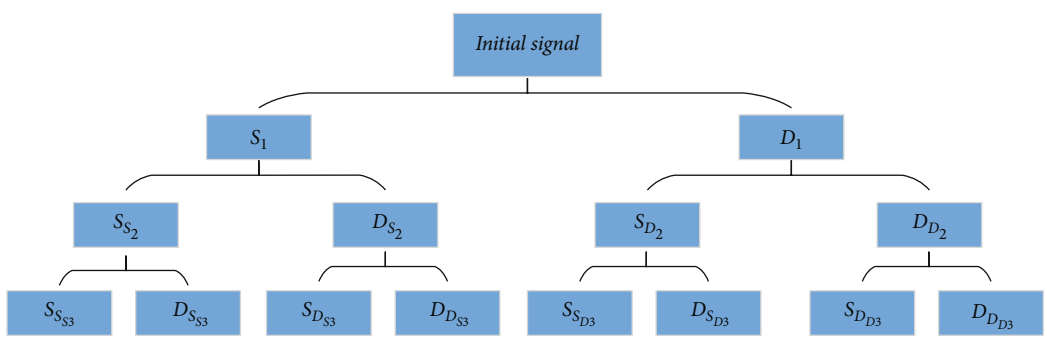

Figure 5: Schematic diagram of wavelet packet decomposition.

The reconstruction equation is

$$p_j^i(t) = 2\left[\sum_k h(t-2k)p_{j+1}^{2i-1}(t) + \sum_k g(t-2k)p_{j+1}^{2i}(t)\right]. \quad (7)$$

The signal sampling frequency is 1 kHz in the Maxwell simulation model. According to the sampling theorem, the maximum frequency is 500 Hz. Since the fault harmonic energy in the signal is much smaller than the fundamental frequency, to separate the fundamental frequency from the fault harmonic, 7-layer wavelet packet decomposition is performed on the A-phase current signal, and 2^7 sub-bands are obtained.

In order to better distinguish the energy between different fault states, the db6 wavelet basis is used, and the decomposition process is shown in Figure 6. Since there are many sub-bands after decomposition, only the sub-band signals of the first 12 dimensions are shown in the figure.

The energy value of the reconstructed signal is calculated according to

$$E_j = \left|\int S_j(t)\right|^2 dt = \sum_{k=1}^{n} \left|x_{jk}\right|^2, j = 0, 1, 2 \cdots 127. \quad (8)$$

E_j is the energy amplitude of each frequency band. x_{jk} is the value of each discrete point.

To avoid the interference caused by the change of energy amplitude of each frequency band under different working conditions, the energy value of each frequency band is normalized. The normalized energy value obtained is shown in Figure 7. Due to the large number of sub-bands obtained by wavelet packet decomposition, only the normalized

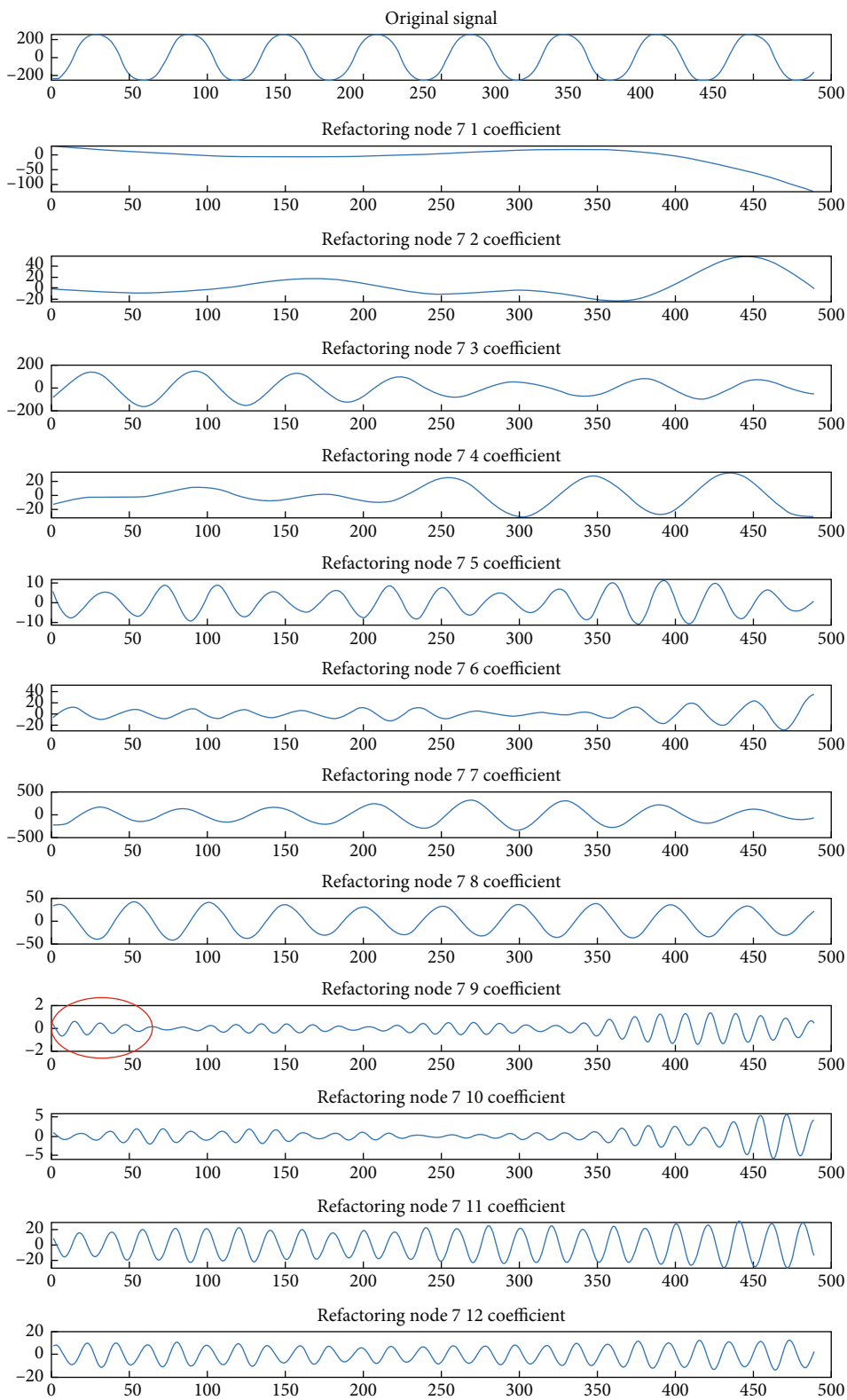

(a) Normal state

Figure 6: Continued.

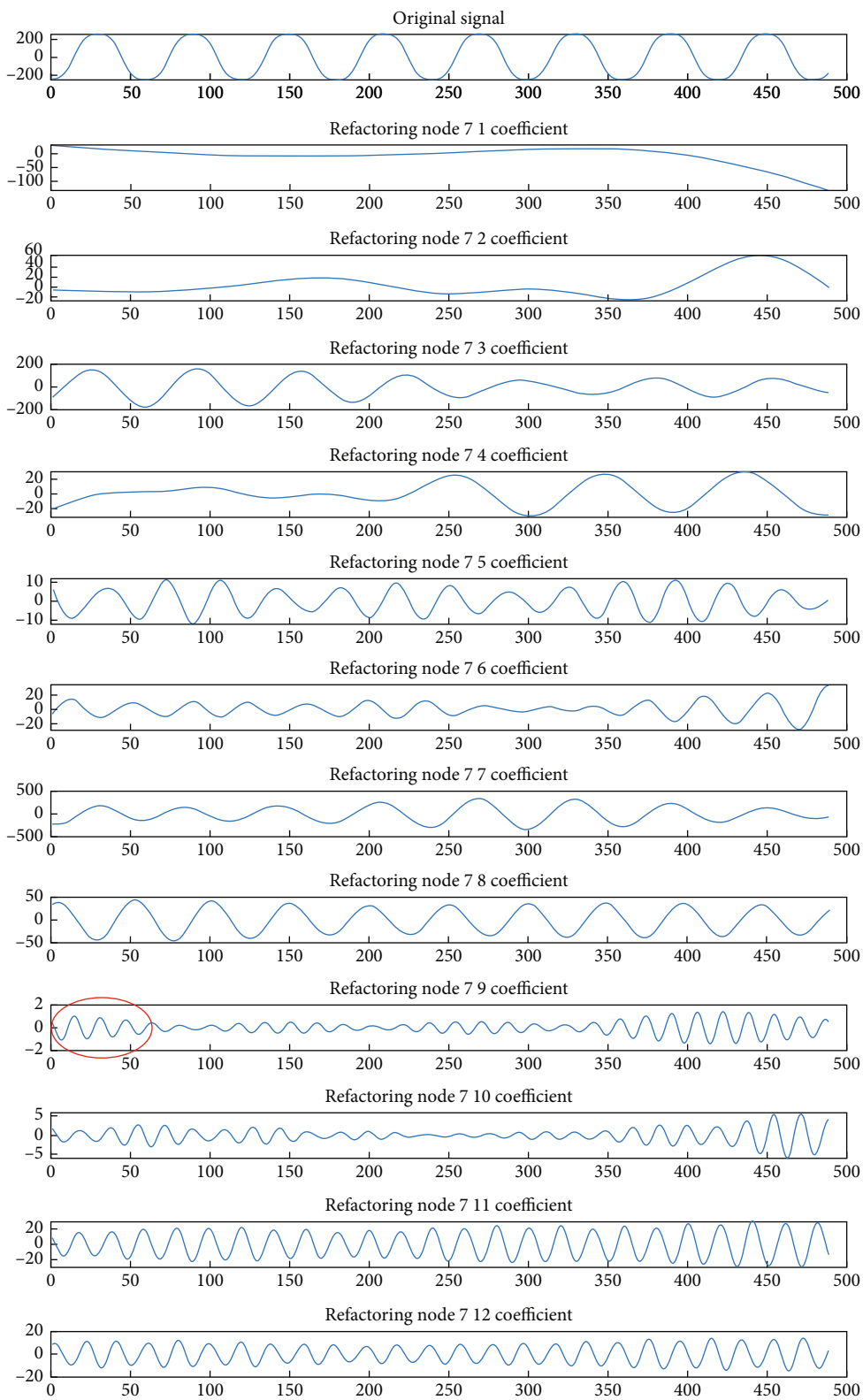

(b) Uniform demagnetization

Figure 6: Continued.

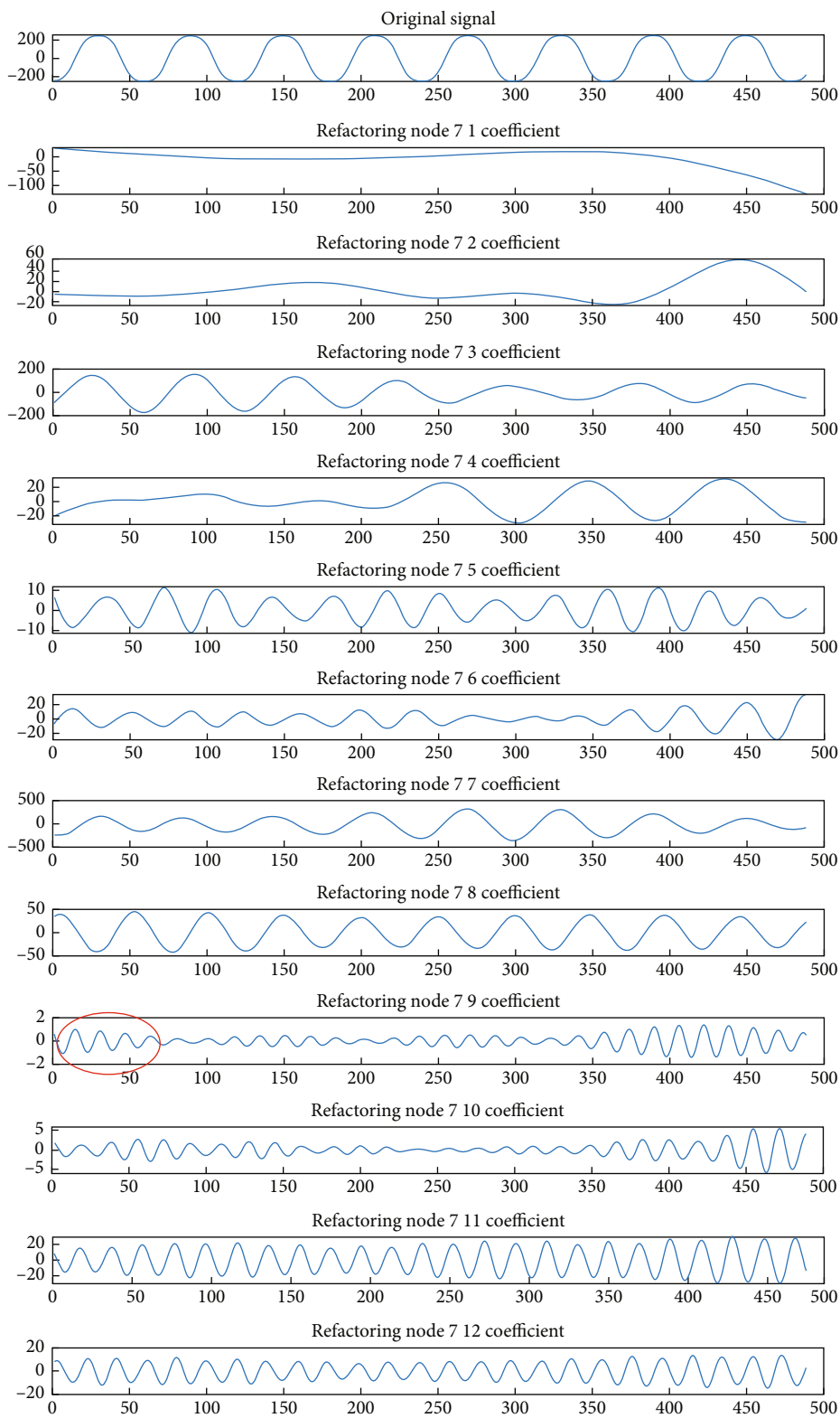

(c) Partial demagnetization

Figure 6: Wavelet packet decomposition process.

energy values of the first nine sub-bands are shown. As can be seen from Figure 7, the energy contained in each frequency band under normal operation and global and local demagnetization is different, and the gap is obvious. The sub-band S7 contains the highest energy. The normalized energies of the three states are 56.35, 54.77, and 55.14,

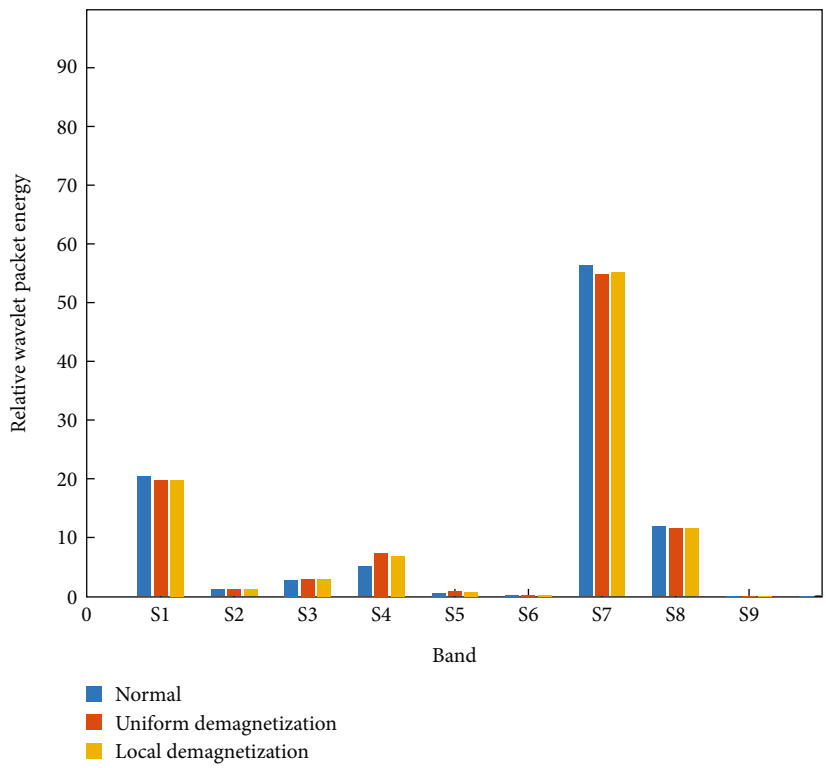

Figure 7: Wavelet packet-normalized band energy.

respectively. The energy difference of the three states in sub-band S4 is the most obvious, which is 5.048, 7.365, and 6.864, respectively. Therefore, it is feasible to extract the degaussing characteristic of A-phase current by wavelet packet analysis.

According to the relevant reference [30], the 10th and above harmonics in the current signal have small signal amplitudes, so the first 40-dimensional wavelet packet energy value is selected as the fault feature vector for subsequent fault classification.

4. Demagnetization Fault Diagnosis Method

SVM is a machine learning algorithm based on the principle of structural risk minimization, which realizes sample classification by solving the optimal hyperplane. It is widely used in regression problems and classification problems. LSSVM is an improved algorithm of SVM, which uses equality constraints instead of inequality constraints in SVM to solve the optimization problem into a linear equation, which greatly reduces the computational complexity. In order to identify the demagnetization fault type of PMSM according to the fault feature vector extracted above, the method of LSSVM is used to realize the discrimination of demagnetization fault type. The flowchart of LSSVM and SVM methods is shown as Figure 8.

4.1. Principle of SVM. For a training set with n points $D = \{(x_i, y_i)\, i = 1, 2, \cdots n\}, x_i \in R^n, y_i \in \{1, -1\}$, it can be binary classified by an optimal plane $H : \omega_x + b = 0$. Two other hyperplanes $H_1 : \omega_x + b = 1$ and $H_2 : \omega_x + b = -1$ are defined. Both H_1 and H_2 are parallel to H, and the minimum distances from H_1 and H_2 to the two types of sample points are 0, respectively, as shown in Figure 9.

The no sample points that exist between H_1 and H_2 should be ensured, that is,

$$\begin{cases} \omega x_i + b \geq 1, & y_i = 1, \\ \omega x_i + b \leq -1, & y_i = -1. \end{cases} \tag{9}$$

Equation (9) can be rewritten as

$$y_i(\omega \cdot x_i + b) - 1 \geq 0, \quad i = 1, 2 \cdots n. \tag{10}$$

To maximize the classification interval $2/\|\omega\|$, the SVM learning task is used:

$$\begin{aligned} &\min_{\omega, b} \frac{1}{2}\|\omega\|^2 = \min_{\omega, b} \frac{1}{2}\omega^T \omega \\ &\text{s.t.} y_i(\omega \bullet x_i + b) - 1 \geq 0, \quad i = 1, 2 \cdots n. \end{aligned} \tag{11}$$

The corresponding Lagrangian function is

$$L(\omega, b, \alpha) = \frac{1}{2}\omega^T \omega - \sum_{i=1}^{n} \alpha_i [y_i(\omega \bullet x_i + b) - 1], \tag{12}$$

where α_i is the Lagrange multiplier.

For problems that are difficult to be classified by a linear hyperplane, a kernel function can be introduced to map the samples to a high-dimensional space, that is, $x \longrightarrow \Phi(x)$,

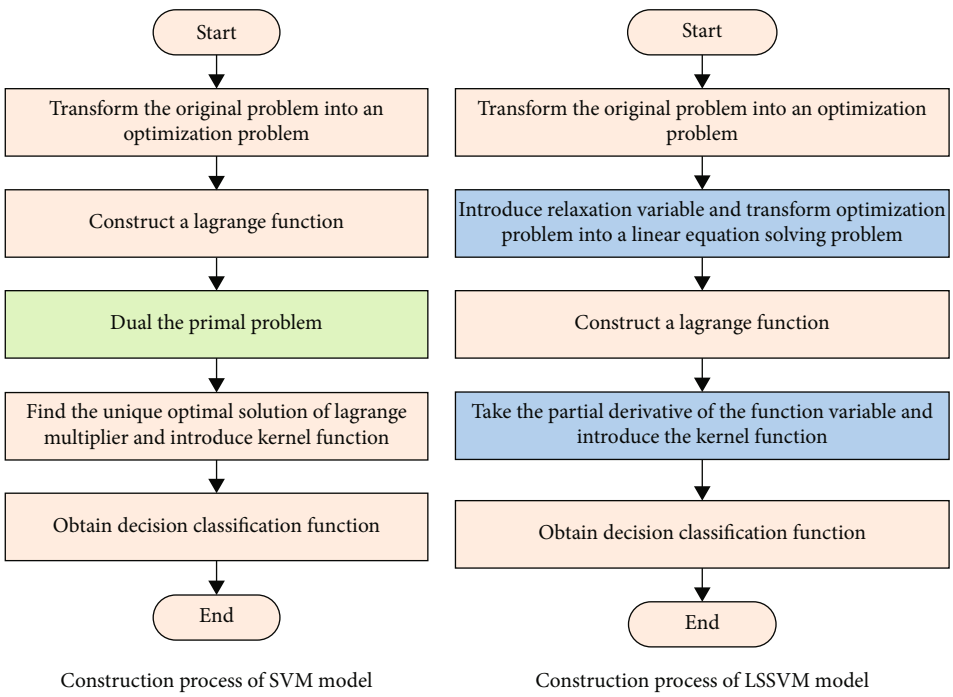

Figure 8: The flowchart of LSSVM and SVM methods.

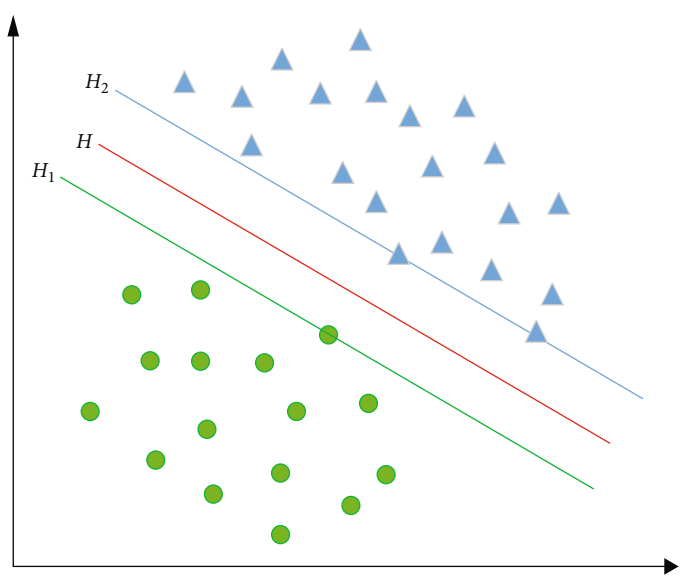

Figure 9: Optimal hyperplane diagram.

$(x_i, y_i) \longrightarrow (\Phi(x), y(i))$, to make the problem linearly separable, as shown in Figure 10.

4.2. Principle of LSSVM. In LSSVM, the slack variable ξ_i can take a negative value, and the optimization problem becomes

$$\min \ \frac{1}{2}\omega^T\omega + \frac{C}{2}\sum_{i=1}^{n}\xi_i \qquad (13)$$
$$\text{s.t.} y_i(\omega \bullet \Phi(x_i) + b) - 1 + \xi_i = 0,$$

where C is the penalty factor, which represents the tolerance to wrong samples.

The Lagrangian function is

$$L(\omega, b, \xi, \alpha) = \frac{1}{2}\omega^T\omega + \frac{C}{2}\sum_{i=1}^{n}\xi_i - \sum_{i=1}^{n}\alpha_i[y_i(\omega \bullet \Phi(x_i) + b) - 1 + \xi_i]. \qquad (14)$$

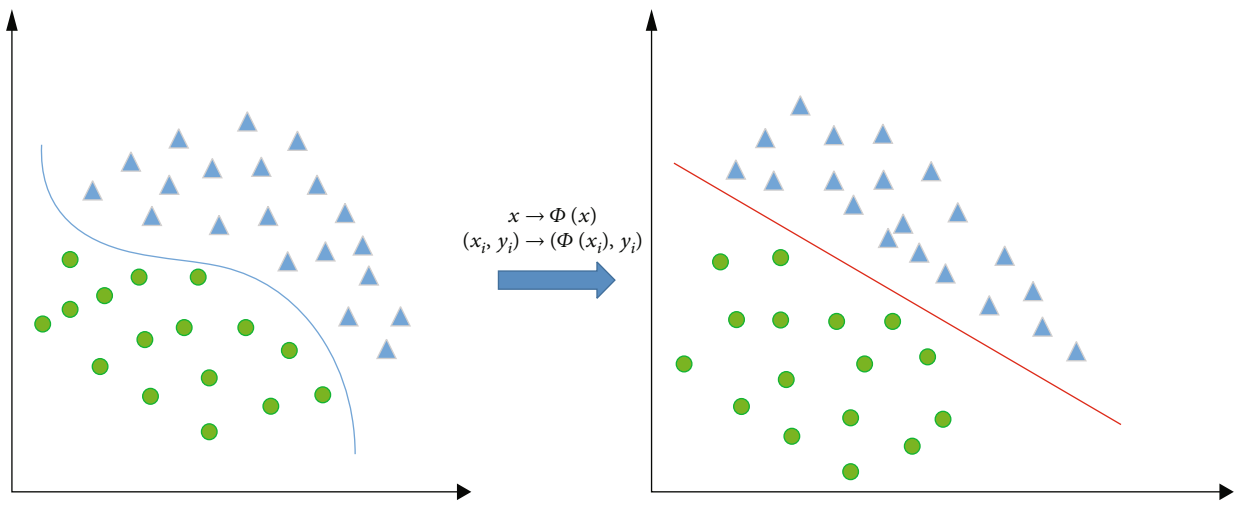

Figure 10: Schematic diagram of SVM dimension transformation.

Let the partial derivatives of the above formula to ω, b, and ξ_i be equal to 0, that is,

$$\begin{cases} \dfrac{\partial L}{\partial \omega} = 0 \Rightarrow \omega = \sum_{i=1}^{n} \alpha_i y_i \Phi(x_i), \\ \dfrac{\partial L}{\partial b} = 0 \Rightarrow \sum_{i=1}^{n} \alpha_i y_i = 0, \\ \dfrac{\partial L}{\partial \xi_i} = 0 \Rightarrow \alpha_i = C\xi_i, \\ \dfrac{\partial L}{\partial \xi_i} = 0 \Rightarrow y_i(\omega \bullet \Phi(x_i) + b) - 1 + \xi_i = 0. \end{cases} \tag{15}$$

Equation (15) is simplified as follows:

$$\begin{bmatrix} I & 0 & 0 & -Z^T \\ 0 & 0 & 0 & -Y^T \\ 0 & 0 & CI & -I \\ Z & Y & I & 0 \end{bmatrix} \begin{bmatrix} \omega \\ b \\ \xi \\ \alpha \end{bmatrix} = \begin{bmatrix} 0 \\ 0 \\ 0 \\ 1 \end{bmatrix}, \tag{16}$$

where

$$\begin{cases} Z = [\Phi(x_1)y_1, \Phi(x_2)y_2 \cdots, \Phi(x_2)y_2]^T, \\ Y = [y_1, y_2, \cdots, y_n]^T, \\ 1_\xi = [1, 1, \cdots, 1]^T, \\ \xi = [\xi_1, \xi_2, \cdots, \xi_n]^T, \\ \alpha = [\alpha_1, \alpha_2, \cdots, \alpha_n]^T. \end{cases} \tag{17}$$

Set $\Omega = ZZ^T$, ω, and ξ are eliminated, and the following equation can be obtained.

$$\begin{bmatrix} 0 & -Y^T \\ Y & \Omega + C^{-1}I \end{bmatrix} \begin{bmatrix} b \\ \alpha \end{bmatrix} = \begin{bmatrix} 0 \\ 1_\xi \end{bmatrix}. \tag{18}$$

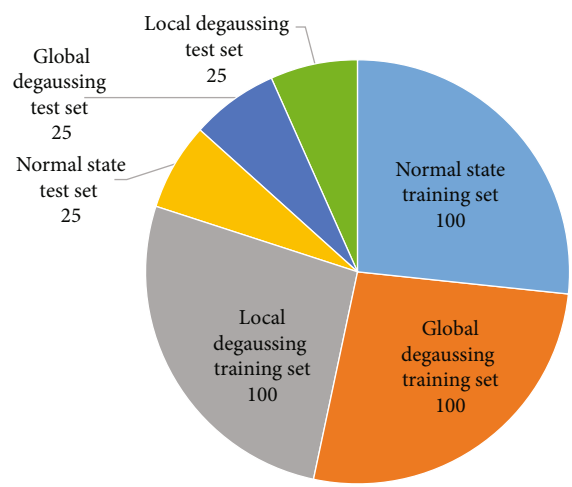

Figure 11: Data set distribution.

The inner product of the feature space $[\Phi(x_i), \Phi(x_j)]$ is replaced by the kernel function $K(x_i, x_j)$.

$$\Omega_{i,j} = y_i y_j \Phi(x_i)^T \bullet \Phi(x_j) = y_i y_j K(x_i x_j). \tag{19}$$

The classification decision function is

$$f(x) = \operatorname{sgn}\left[\sum_{i=1}^{n} \alpha_i y_i K(x, x_i) + b\right]. \tag{20}$$

The A-phase current data in three states of normal, uniform demagnetization, and partial demagnetization are collected. The demagnetization feature quantity is extracted.

Input is the first 40-dimensional wavelet packet energy value. There are 125 groups of samples in the three states, of which 100 groups are training samples and 25 groups are test samples. The specific distribution is shown in Figure 11. The output is the diagnostic result shown in Table 2. The previous 40-dimensional wavelet packet energy

Table 2: Partial sample eigenvector.

Number	E_1	E_2	E_3	E_4	E_5	E_6	E_7	E_8
1	20.3937	1.1228	2.7706	5.0482	0.5553	0.2233	56.3504	11.8921
2	20.3901	1.1226	2.7706	5.0508	0.5524	0.2233	56.3514	11.8928
3	19.6515	1.1074	2.9345	7.3652	0.7712	0.2160	54.7725	11.4718
4	19.6421	1.1070	2.9345	7.3709	0.7682	0.2160	54.7773	11.4741
5	19.6406	1.1069	2.9345	7.3719	0.7678	0.2160	54.7780	11.4745
6	19.6406	1.1069	2.9345	7.3722	0.7677	0.2160	54.7779	11.4745
7	19.7628	1.1083	2.9005	6.8642	0.7246	0.2174	55.1419	11.5664
8	19.7558	1.1079	2.9005	6.8683	0.7225	0.2174	55.1456	11.5682
9	19.7545	1.1079	2.9005	6.8690	0.7223	0.2174	55.1463	11.5684
10	19.7543	1.1079	2.9005	6.8691	0.7223	0.2174	55.1464	11.5684

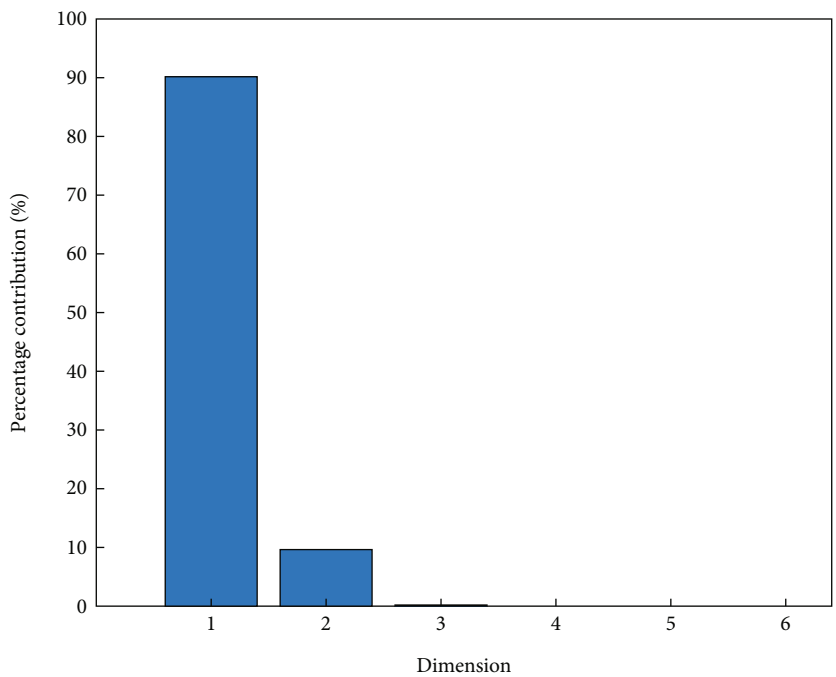

Figure 12: Contribution of the first five dimensions of data.

value was used as the fault feature vector, and the data set was established as shown in Table 2. The data set was divided into training set and test set. PCA replaces the original N features with a smaller number of K features. The new features are linear combinations of the old features. These linear combinations maximize the sample variance and make the new K features as independent as possible. The specific steps are as follows: (1) the sample mean and standard deviation of each index are calculated. (2) The sample is standardized and its standardized matrix is calculated. (3) According to the obtained standardized matrix, the correlation coefficient matrix is calculated. (4) The eigenvalues are solved. The range of K is determined according to the contribution rate of cumulative variance, and K principal components are established. (5) The feature vector set of principal component whose feature contribution rate is greater than 95% is selected. After PCA dimensionality reduction of the data set, SVM or LSSVM was trained using the training set, and the trained SVM or LSSVM was used for fault diagnosis classification. The first 8-dimensional feature vectors of some samples are shown in Table 2. Groups 1 and 2 are eigenvectors under normal conditions. Groups 3-6 are eigenvectors under partial demagnetization faults. Groups 7-10 are eigenvectors under uniform demagnetization faults.

In order to improve the recognition accuracy, the energy value is reduced in dimension. The dimensionality reduction of the demagnetization feature can not only reflect the original data with low-dimensional data but also eliminate redundant data from the excessive demagnetization feature, reduce the calculation amount, improve the recognition rate, and make the subsequent classification results stable and effective.

PCA is a common method of data dimensionality reduction, which transforms the original data from n-dimensional

Table 3: SVM comprehensive test results.

Kernel function	Motor status	Number of test samples	Number of correct classifications	Number of misclassifications	Correct rate	Total correct rate
Linear	Normal	25	23	2	92%	90.67%
	Uniform demagnetization	25	24	1	96%	
	Partial demagnetization	25	21	4	84%	
Polynomial	Normal	25	23	2	92%	89.33%
	Uniform demagnetization	25	24	1	96%	
	Partial demagnetization	25	20	5	80%	
Radial basis	Normal	25	23	2	92%	88%
	Uniform demagnetization	25	24	1	96%	
	Partial demagnetization	25	19	6	86%	

Table 4: LSSVM comprehensive test results.

Kernel function	Motor status	Number of test samples	Number of correct classifications	Number of misclassifications	Correct rate	Total correct rate
Linear	Normal	25	24	1	96%	98.67%
	Uniform demagnetization	25	25	0	100%	
	Partial demagnetization	25	25	0	100%	
Polynomial	Normal	25	23	2	92%	92%
	Uniform demagnetization	25	24	1	96%	
	Partial demagnetization	25	22	3	88%	
Radial basis	Normal	25	25	0	100%	94.67%
	Uniform demagnetization	25	23	2	92%	
	Partial demagnetization	25	23	2	92%	

space to m-dimensional linear space by solving the eigenvectors of the covariance matrix of the original data. The PCA method is used to reduce the dimensionality of the fault feature vector, and the first 5-dimensional data are selected for subsequent fault classification according to the principle that the sum of the contributions of the selected dimensional data is greater than 95%. The contribution of the first 5-dimensional data is shown in Figure 12.

In order to verify the advantages of the LSSVM, we also use the traditional SVM to classify the signal. SVM and LSSVM classification and recognition are performed on the data after PCA dimensionality reduction, respectively. The kernel functions are linear, polynomial, and radial basis kernel functions, respectively. The grid search method is used for the specific parameters in the model. The test results are shown in Tables 3 and 4. The results shows that the accuracy of classification and recognition with LSSVM and SVM is basically similar, and the accuracy of LSSVM method is slightly higher. At the same time, the accuracy of the radial basis kernel function is higher.

In order to further analyze the research results, the confusion matrix is obtained, as shown in Figure 13.

Therefore, the LSSVM is finally used to classify and test the data after wavelet packet decomposition and PCA dimension reduction, where $c = 9.7656e - 4$ and $g = 1.4641$. The results show that the judgment error of the method proposed for the type of demagnetization fault does not exceed 10%, which shows that the method has a good effect on the

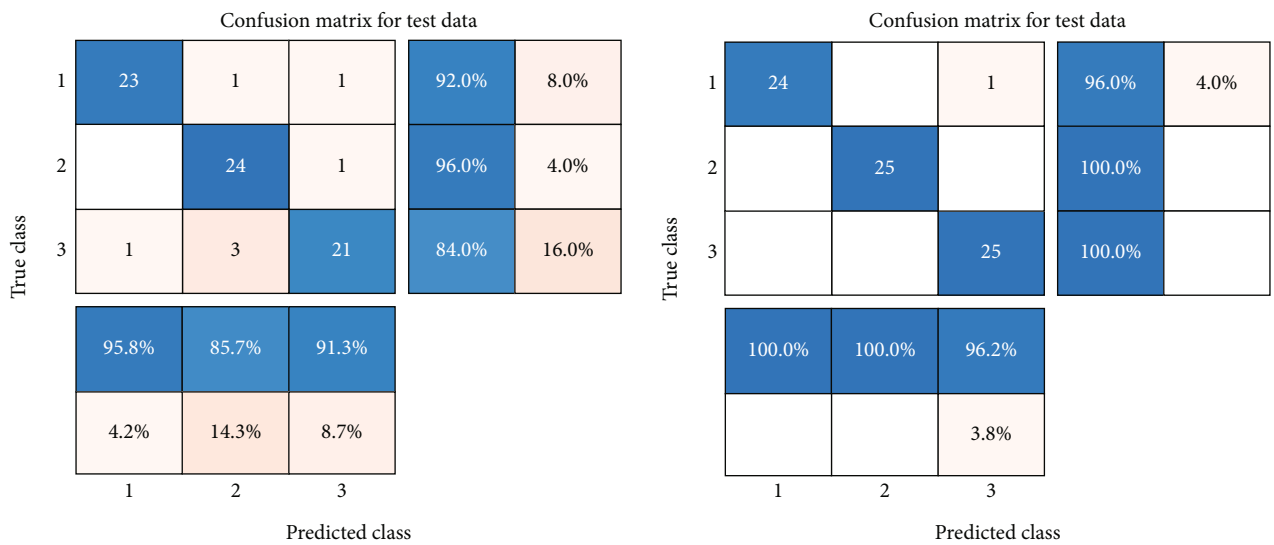

Figure 13: Confusion matrix of SVM and LSSVM.

classification of demagnetization faults. Compared with the accuracy of existing studies (MGWO-SVM/correct rate 96.5% [31], IPSO-LSSVM/correct rate 96.7% [32]), the LSSVM based on linear kernel function in this paper has a higher accuracy (98.67%) for the classification and diagnosis of permanent magnet demagnetization faults.

5. Conclusion

The two-dimensional simulation model of PMSM under normal state, uniform demagnetization, and partial demagnetization faults was established based on the Maxwell simulation platform by using the time-step finite element method. The A-phase current in the simulation process is collected and demagnetized by 7-layer wavelet packet decomposition to extract the demagnetization feature quantities that can characterize different demagnetization fault types. Finally, based on PCA dimensionality reduction and LSSVM, the classification of demagnetization feature quantities under different demagnetization fault types is realized. The research results show that the classification accuracy can reach more than 90%, which has important significance for the judgment of PMSM permanent magnet demagnetization fault types. The results show that the classification accuracy is high when the kernel function is linear. Compared with SVM, LSSVM has higher accuracy and is more suitable for classification diagnosis of demagnetization faults.

Data Availability

Some or all data generated or used during the study are available from the corresponding author by request.

Conflicts of Interest

The authors declare no conflict of interest.

Acknowledgments

This work is supported by the National Natural Science Foundation of China (Grant No. 52375250), the Basic Research Program of Xuzhou City (Grant No. KC22023), and the University Synergy Innovation Program of Anhui Province (Grant No. GXXT-2022-019).

References

[1] S. S. Moosavi, A. Djerdir, Y. A. Amirat, and D. A. Khaburi, "Demagnetization fault diagnosis in permanent magnet synchronous motors: a review of the state-of-the-art," *Journal of Magnetism and Magnetic Materials*, vol. 391, pp. 203–212, 2015.

[2] L. C. Sheng, W. Li, Y. Q. Wang, M. B. Fan, and X. F. Yang, "Sensorless control of a shearer short-range cutting interior permanent magnet synchronous motor based on a new sliding mode observer," *Ieee Access*, vol. 5, pp. 18439–18450, 2017.

[3] L. C. Sheng, W. Li, Y. Q. Wang, M. B. Fan, and X. F. Yang, "Nonlinear dynamic analysis and chaos control of multi-freedom semi-direct gear drive system in coal cutters," *Mechanical Systems and Signal Processing*, vol. 116, pp. 62–77, 2019.

[4] S. Chakraborty, E. Keller, A. Ray, and J. Mayer, "Detection and estimation of demagnetization faults in permanent magnet synchronous motors," *Electric Power Systems Research*, vol. 96, pp. 225–236, 2013.

[5] R. Z. Haddad, C. A. Lopez, S. N. Foster, and E. G. Strangas, "A voltage-based approach for fault detection and separation in permanent magnet synchronous machines," *IEEE Transactions on Industry Applications*, vol. 53, no. 6, pp. 5305–5314, 2017.

[6] H. W. He, N. N. Zhou, J. Q. Guo, Z. Zhang, B. Lu, and C. Sun, "Tolerance analysis of electrified vehicles on the motor demagnetization fault: from an energy perspective," *Applied Energy*, vol. 227, pp. 239–248, 2018.

[7] Z. J. Liu, J. Huang, and B. N. Li, "Diagnosing and distinguishing rotor eccentricity from partial demagnetisation of interior

PMSM based on fluctuation of high-frequency d-axis inductance and rotor flux," *IET Electric Power Applications*, vol. 11, no. 7, pp. 1265–1275, 2017.

[8] J. C. Urresty, J. R. Riba, M. Delgado, and L. Romeral, "Detection of demagnetization faults in surface-mounted permanent magnet synchronous motors by means of the zero-sequence voltage component," *IEEE Transactions on Energy Conversion*, vol. 27, no. 1, pp. 42–51, 2012.

[9] S. Ruoho, M. Haavisto, E. Takala, T. Santa-Nokki, and M. Paju, "Temperature dependence of resistivity of sintered rare-earth permanent-magnet materials," *IEEE Transactions on Magnetics*, vol. 46, no. 1, pp. 15–20, 2010.

[10] J. C. Urresty, J. R. Riba, and L. Romeral, "A back-emf based method to detect magnet failures in PMSMs," *IEEE Transactions on Magnetics*, vol. 49, no. 1, pp. 591–598, 2013.

[11] M. Zhu, W. S. Hu, and N. C. Kar, "Torque-ripple-based interior permanent-magnet synchronous machine rotor demagnetization fault detection and current regulation," *IEEE Transactions on Industry Applications*, vol. 53, no. 3, pp. 2795–2804, 2017.

[12] M. Zhu, B. Yang, W. S. Hu, G. D. Feng, and N. C. Kar, "Vold-Kalman filtering order tracking based rotor demagnetization detection in PMSM," *IEEE Transactions on Industry Applications*, vol. 55, no. 6, pp. 5768–5778, 2019.

[13] C. Wang, M. D. Prieto, L. Romeral, Z. Chen, F. Blaabjerg, and X. Liu, "Detection of partial demagnetization fault in PMSMs operating under nonstationary conditions," *Ieee Transactions on Magnetics*, vol. 52, no. 7, 2016.

[14] A. G. Espinosa, J. A. Rosero, J. Cusido, L. Romeral, and J. A. Ortega, "Fault detection by means of Hilbert-Huang transform of the stator current in a PMSM with demagnetization," *IEEE Transactions on Energy Conversion*, vol. 25, no. 2, pp. 312–318, 2010.

[15] B. M. Ebrahimi and J. Faiz, "Demagnetization fault diagnosis in surface mounted permanent magnet synchronous motors," *IEEE Transactions on Magnetics*, vol. 49, no. 3, pp. 1185–1192, 2013.

[16] J. C. Urresty, R. Atashkhooei, J. R. Riba, L. Romeral, and S. Royo, "Shaft trajectory analysis in a partially demagnetized permanent-magnet synchronous motor," *IEEE Transactions on Industrial Electronics*, vol. 60, no. 8, pp. 3454–3461, 2013.

[17] J. De Bisschop, A. Abdallh, P. Sergeant, and L. Dupre, "Identification of demagnetization faults in axial flux permanent magnet synchronous machines using an inverse problem coupled with an analytical model," *Ieee Transactions on Magnetics*, vol. 50, no. 11, 2014.

[18] X. G. Li, Y. Z. Zhang, F. Q. Wang, and S. Sun, "A fault diagnosis method of rolling bearing based on wavelet packet analysis and deep forest," *Symmetry*, vol. 14, no. 2, 2022.

[19] S. C. Xiong, H. D. Zhou, S. He, L. L. Zhang, and T. L. Shi, "Fault diagnosis of a rolling bearing based on the wavelet packet transform and a deep residual network with lightweight multi-branch structure," *Measurement Science and Technology*, vol. 32, no. 8, article 085106, 2021.

[20] M. H. Zhao, X. Y. Fu, Y. J. Zhang, L. H. Meng, and B. P. Tang, "Highly imbalanced fault diagnosis of mechanical systems based on wavelet packet distortion and convolutional neural networks," *Advanced Engineering Informatics*, vol. 51, article 101535, 2022.

[21] Z. Kuai and G. Huang, "Fault diagnosis of diesel engine valve clearance based on wavelet packet decomposition and neural networks," *Electronics*, vol. 12, no. 2, p. 353, 2023.

[22] M. Krichen, E. Elbouchikhi, N. Benhadj, M. Chaieb, M. Benbouzid, and R. Neji, "Motor current signature analysis-based permanent magnet synchronous motor demagnetization characterization and detection," *Machines*, vol. 8, no. 3, 2020.

[23] M. Krichen, N. Ben Halima, D. Abdeljalil, N. Ben Hadj, and R. Neji, "Investigation of the combined static eccentricity and partial demagnetization faults in PMSM," in *2022 IEEE 21st international Ccnference on Sciences and Techniques of Automatic Control and Computer Engineering (STA)*, pp. 648–653, Sousse, Tunisia, 2022.

[24] R. Z. Haddad and E. G. Strangas, "On the accuracy of fault detection and separation in permanent magnet synchronous machines using MCSA/MVSA and LDA," *IEEE Transactions on Energy Conversion*, vol. 31, no. 3, pp. 924–934, 2016.

[25] M. Fitouri, M. N. Abdelkrim, and Y. B. Salem, "Diagnosis of stator faults in permanent magnet synchronous machine using finite element method," *International Journal of Digital Signals and Smart Systems*, vol. 3, no. 4, p. 187, 2019.

[26] J. Z. Zhang, J. Hang, and M. Cheng, "Diagnosis of mechanical unbalance fault in permanent magnet synchronous machine drives," *Electric Power Components and Systems*, vol. 44, no. 12, pp. 1408–1417, 2016.

[27] X. J. Song, J. T. Hu, H. Y. Zhu, and J. L. Zhang, "A bearing outer raceway fault detection method in induction motors based on instantaneous frequency of the stator current," *IEEJ Transactions on Electrical and Electronic Engineering*, vol. 13, no. 3, pp. 510–516, 2018.

[28] T. Ishikawa and N. Igarashi, "Failure diagnosis of demagnetization in interior permanent magnet synchronous motors using vibration characteristics," *Applied Sciences-Basel*, vol. 9, no. 15, p. 3111, 2019.

[29] M. Zhu, W. S. Hu, and N. C. Kar, "Acoustic noise-based uniform permanent-magnet demagnetization detection in SPMSM for high-performance PMSM drive," *IEEE Transactions on Transportation Electrification*, vol. 4, no. 1, pp. 303–313, 2018.

[30] M. Zhang, *Study on Fault Recognition of Permanent Magnet Synchronous Machine Based on Multi-Source Information Fusion, [M.S. thesis]*, Chongqing University, Chongqing, 2018.

[31] L. L. Li, J. Q. Liu, W. B. Zhao, and L. Dong, "Fault diagnosis of high-speed brushless permanent-magnet dc motor based on support vector machine optimized by modified grey wolf optimization algorithm," *Symmetry*, vol. 13, no. 2, p. 163, 2021.

[32] L. Wang, W. W. Li, L. Zhang, and J. Liu, "Fault diagnosis of motor rotor based on IPSO-LSSVM with hybrid kernel function," in *Electronics, Electrical Engineering and Information Science*, pp. 874–887, World Scientific, 2016.